

Article

Magnetite @ Zinc Cobalt Ferrite Nanoparticles: Synthesis, Magnetic Behavior, and Optical Properties

Mohamed S. A. Darwish 

Egyptian Petroleum Research Institute, 1 Ahmed El-Zomor Street, El Zohour Region, Nasr City, Cairo 11727, Egypt; msa.darwish@gmail.com

Abstract: One of the main challenges is using an effective photocatalyst that responds to a broad range of visible light for hydrogen production during water splitting. Series types of photocatalysts based on magnetic ferrite nanostructure were fabricated via a two-step co-precipitation technique. Precisely, four types of magnetic structures: magnetite nanoparticles (MNPs), zinc cobalt ferrite nanoparticles (ZCFNPs), hybrid magnetite/zinc cobalt ferrite nanoparticles (MNPs @ ZCFNPs), and hybrid zinc cobalt ferrite/magnetite nanoparticles (ZCFNPs @ MNPs) were used to fabricate magnetic photocatalysts. The characterizations of the fabricated magnetic photocatalysts were investigated via TEM, zeta potential, XRD, VSM, and UV-VIS spectroscopy. ZCFNPs @ MNPs showed the smallest particle with size ≈ 11 nm. The magnetization value of ZCFNPs @ MNPs (59.3 emu/g) was improved compared to the MNPs (41.93 emu/g). The produced hydrogen levels via photocatalyst were 60, 10, 24, and 1.4 mmole $\text{min}^{-1} \text{g}^{-1}$ for MNPs, ZCFNPs, MNPs @ ZCFNPs, and ZCFNPs @ MNPs, respectively, under visible light with magnetic force. MNPs displayed outstanding performance as magnetic photocatalysts for the water-splitting process.

Keywords: magnetic ferrite; zinc cobalt ferrite nanoparticles; nanostructure; photocatalysts



Citation: Darwish, M.S.A. Magnetite @ Zinc Cobalt Ferrite Nanoparticles: Synthesis, Magnetic Behavior, and Optical Properties. *Crystals* **2023**, *13*, 1284. <https://doi.org/10.3390/cryst13081284>

Academic Editor: Nabeen K Shrestha

Received: 27 June 2023

Revised: 16 August 2023

Accepted: 18 August 2023

Published: 20 August 2023



Copyright: © 2023 by the author. Licensee MDPI, Basel, Switzerland. This article is an open access article distributed under the terms and conditions of the Creative Commons Attribution (CC BY) license (<https://creativecommons.org/licenses/by/4.0/>).

1. Introduction

Ferrites nanostructure with the formula $M\text{-Fe}_2\text{O}_4$ ($M = \text{Fe, Zn, Co}$) has been considered of interest due to their unparalleled structure, outstanding magnetic behavior, chemical stability, and lower expense [1–3]. The magnetic nanostructures are used as catalysts and can be fabricated via varied techniques as hydrothermal, electro-deposition, sol-gel, and co-precipitation methods [4–11]. The co-precipitation process is a promising technique for the expansion of a stabilized, inexpensive, reproducible, and attainable path for the large fabrication of a magnetic ferrites nanostructure as efficient catalysts. The most challenging and promising outlet in energy production is the generation of clean and renewable energy [5–9]. The production of hydrogen has received a lot of attention as a clean energy source with high energy content. Production of hydrogen today uses a variety of methods [1,2]. Hydrogen production using photocatalytic via the water-splitting method is more favorable than the other techniques as a simple method with lower required energy [4,5]. Among spinel ferrites, cobalt ferrite is of great interest for their outstanding chemical and mechanical constancy, elevated coercivity, and high magneto-crystalline anisotropy [12,13]. Cobalt ferrite nanostructure has acquired high interest due to its behavior, such as elevated surface area and quantum yield, with outstanding photostability [14]. As the size of the magnetic particles decreased to the nano-domain, the magnetic properties of the particles relatively decreased due to the high surface area, size of the quantum effect, and interaction between the magnetic particles. The presence of the bi-magnetic nanostructure as a photo-material is proper in the splitting of the water process. The hydrogen yields could be enhanced with the inner-magnetic behavior of the photocatalyst. The presence of two types of oxides in the nanostructured matrix is remarkable due to the presence of oxygen vacancies in the structures [15,16]. The coating

with cobalt ferrite nanoparticles through the chemical precipitation process could influence the photocatalytic behavior of the magnetite nanoparticles in the production of hydrogen. Nanostructures based on cobalt/iron oxide nanoparticles were used as photocatalysts for the production of hydrogen. Controlling the size of nanoparticles can considerably tune its magnetic-photo behavior. The cobalt ferrite nanoparticles on the magnetite NPs act as co-catalysts. This is efficient as electrons trap the electrons outgoing to the magnetite NPs, thereby preventing the re-grouping of the hole with electrons. It possibly promotes photocatalytic capacity by extending reaction sites on the magnetite NPs and also increases the electron's lifetime [17–20]. The aim of this work was to prepare bi-magnetic hybrid nanoparticles with high photocatalytic performance using a controlled co-precipitation process. Various types of magnetic ferrite nanoparticles were used, namely, magnetite nanoparticles (MNPs), zinc cobalt ferrite nanoparticles (ZCFNPs), hybrid magnetite/zinc cobalt ferrite nanoparticles (MNPs @ ZCFNPs), and hybrid zinc cobalt ferrite/magnetite nanoparticles (ZCFNPs @ MNPs), in order to fabricate visible light-effective photocatalyst in the presence of magnetic force.

2. Materials and Methods

2.1. Materials

Ferric chloride, ferrous chloride, cobalt chloride, zinc chloride, and ammonium hydroxide were ordered from Sigma-Aldrich (St. Louis, MO, USA).

2.2. Fabrication of Bi-Magnetic Hybrid Nanoparticles

The hybrid nanoparticles were fabricated via a two-step coprecipitation technique. Firstly, MNPs and ZCFNPs were prepared (Table 1). Starting materials were dispersed in distilled water (50 mL) and mixed for 15 min. The temperature was risen to 60 °C for 5 min for full homogeneity. Ammonium hydroxide (20 mL) was added with stirring for 30 min at 60 °C. The product was then washed several times with distilled water. NPs were removed from the system via a magnetic field and were dried for 24 h. Secondly, coating on the prepared NPs with a layer was performed, and the same step mentioned above was utilized with the coated materials.

Table 1. Fabrication compositions of bi-magnetic hybrid nanoparticles.

Sample	Nanoparticle Type	NPs	Precursors						
			Coated	Fe ³⁺ (Mole)	Fe ²⁺ (Mole)	DW (mL)	Co ²⁺ (Mole)	Zn ²⁺ (Mole)	Amm. (mL)
A	Magnetite nanoparticles (MNPs)	Fe ₃ O ₄	-	0.59	0.399	50	-	-	20
B	Zinc cobalt ferrite nanoparticles (ZCFNPs)	ZnCoFe ₂ O ₄	-	0.59	0.399	50	0.199	0.199	20
C	Hybrid magnetite/zinc cobalt ferrite nanoparticles (MNPs @ ZCFNPs)	ZnCoFe ₂ O ₄ (0.3 g)	Fe ₃ O ₄	0.149	0.098	25	-	-	5
D	Hybrid zinc cobalt ferrite/magnetite nanoparticles (ZCFNPs @ MNPs)	Fe ₃ O ₄ (0.3 g)	ZnCoFe ₂ O ₄	0.149	0.098	50	0.048	0.049	5

2.3. Hydrogen Production Procedures

The fabricated photocatalyst (0.5 g) was added to the mixture of water/methanol (1:1 by weight). The system was de-gassed via N₂ for 15 min. After that, it was exposed to visible light of power (500 W) with stirring. The intensity of the radiation power was 0.13 W/mL at room temperature under magnetic forces. The obtained gases were collected and studied using GC analysis. The reaction was repeated and triplicated to sure the consistency of the obtained yields.

2.4. Characterization

XRD of the materials was investigated using an X-ray diffractometer (Rigaku, Japan) at a scan speed ($4^\circ/\text{min}$) in the range of 20° to 70° . Zeta potential was studied using Particle size Analyzer (ELSZ-2000; Photal Otsuka Electronics, Osaka, Japan). UV spectroscopic analysis was performed via a UV spectrophotometer (V-570, JASCO, Tokyo, Japan). The magnetic behavior was investigated using VSM (Lake Shore 7400 series; Lake Shore Cryotronics, Westerville, OH, USA). The size of the nanoparticles was investigated using TEM (JEM-2100 LaB6, JEOL, Akishima, Tokyo, Japan).

3. Results and Discussion

3.1. Nanostructures Preparation

Tuning the structure and particle size of fabricated nanoparticles plays a definite role in magnetic and optical properties, which is important for improving the photo activity of the nanostructures. In this work, hybrid nanoparticles, i.e., ZCFNPs @ MNPs and MNPs @ ZCFNPs, were fabricated using a controlled coprecipitation process. It was remarkable to note that the fabricated photo-catalysts were recovered from the system via a simple magnetic separation using a magnet bar.

3.2. The Particle Sizes and Morphologies of the Prepared Nanostructures

The phases and estimated crystallite sizes (nm) of the fabricated nanostructures were investigated using XRD (Figure 1). The crystalline phases of nanostructures were identified with JCPDS data (#221086) (Figure 1) [21]. The indexed peaks at (220), (311), (222), (400), (511), and (440) for the ferrite structure were approved for the fabricated nanostructures. The peaks corresponded to the standard pattern for the dominant magnetite nanoparticles phase (Fe_3O_4). The presence of the second phase was detected in XRD patterns (around 31 and 47 of 2θ). However, the peak may correspond to $\alpha\text{-Fe}_2\text{O}_3$, where Fe_3O_4 is easily oxidized in open conditions [22]. The spinel structures of magnetite, maghemite, and cobalt ferrite are ferrimagnetic structures.

The peaks were weak, probably for disorder/small crystallite effect. The crystallite size (nm) was estimated via the broadening of the most intense and characterized diffraction maxima (311) (Table 2) by using the Scherrer equation:

$$\text{Crystallite size} = K\lambda / (B\cos\theta)$$

D_p (size), B (FWHM), λ (1.5406 Å), K (0.89), and θ (peak position).

MNPs @ ZCFNPs showed the largest crystallite size (≈ 12 nm), and ZCFNPs @ MNPs showed the smallest size (≈ 9 nm). The crystallite size increased with a decrease in the lattice parameter (8.39 Å) for MNPs @ ZCFNPs, by the formation of an amorphous layer of iron oxide surrounding NPs/fractional dissolution of the NP surfaces [23].

The sizes and morphologies of the hybrid nanoparticles were studied via TEM (Figure 2). The particles were aggregated due to the high surface energy and dipole–dipole interactions [24,25]. The TEM showed hybrid nanoparticles, but it did not provide a good contrast between zinc-cobalt ferrite and magnetite. So, it is also possible that two different spinel phases with bimodal distribution in C and D samples may likely be presented. The error in investigating the size was lowered by considering a large number of particles. ZCFNPs had the largest particle size (≈ 25 nm), and they exhibited a polydisperse character with a tendency to form groups, while MNPs had the smallest size (≈ 10 nm). The size of the hybrid nanoparticles can be lower in size than NPs due to the partial dissolution of the nanoparticle surface or lower in aggregation between particles by the presence of a thin coated shell [23].

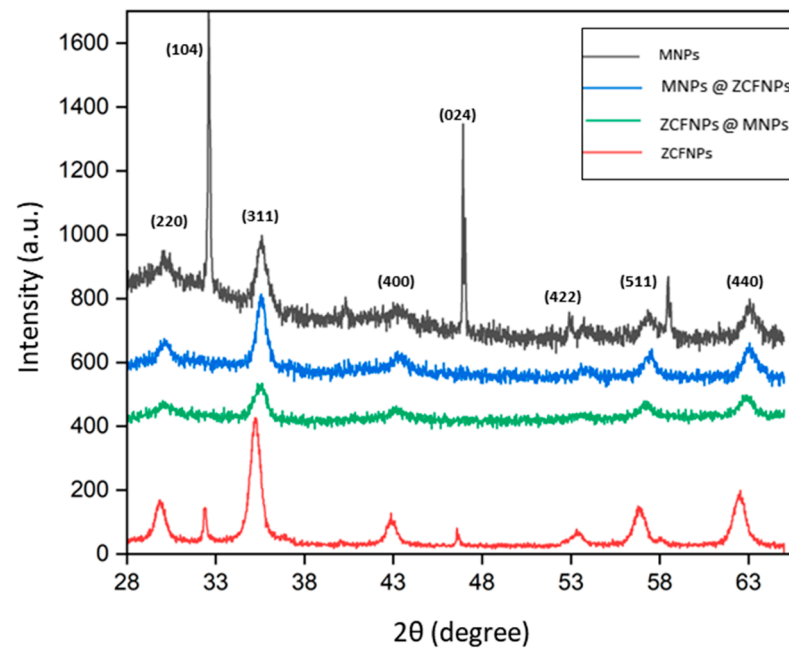


Figure 1. XRD of MNPs, ZCFNPs, MNPs @ ZCFNPs, and ZCFNPs @ MNPs.

Table 2. The size and zeta potential of the nanoparticles.

Sample	MNPs	ZCFNPs	MNPs @ ZCFNPs	ZCFNPs @ MNPs
Crystallite size (nm)	9.8	9.7	12.32	9.44
Particle diameter (nm)	10 ± 0.3	25 ± 5	13 ± 5	11 ± 3
Zeta potential (mV)	$+0.45 \pm 0.2$	$+15 \pm 0.6$	-26 ± 0.5	-4 ± 0.3

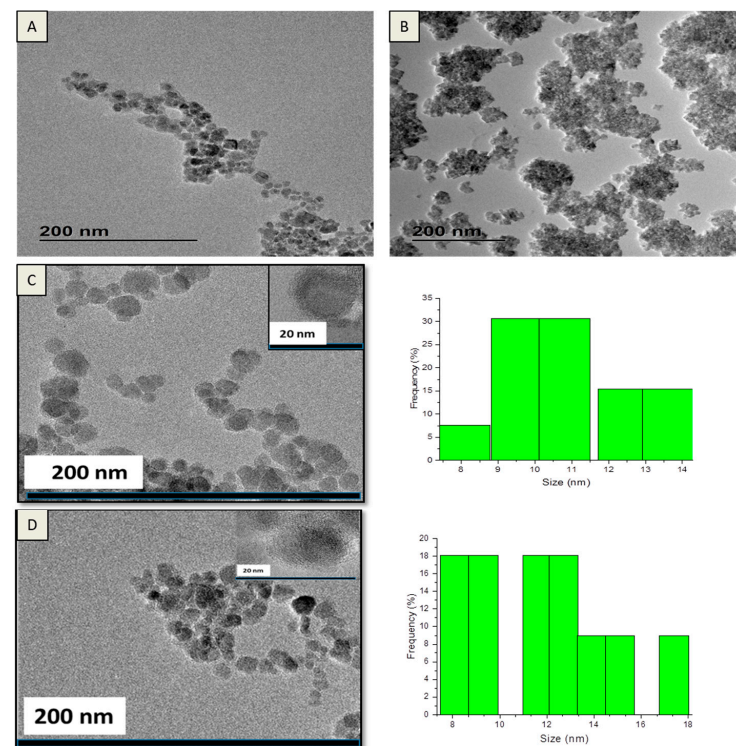


Figure 2. TEM of (A) MNPs (B) ZCFNPs, (C) ZCFNPs @ MNPs, and (D) MNPs @ ZCFNPs.

Zeta potential was investigated, as it was found to be related to the stability of the colloidal solution and accumulation of the NPs, as shown in Figure 3. Photocatalysts for hydrogen production via water photolysis should use a stable and inexpensive visible light absorber able to produce photons with sufficient power for water splitting. The highest zeta potential (ζ) was detected for MNPs @ ZCFNPs (-26 mV), while MNPs obtained the lowest one ($+0.45$ mV) (Table 2). The lower zeta value of MNPs revealed that the particles may display low stability in an aqueous solution. A low value (lower than 5 mV) will enhance the Van der Waals inter-particle attraction, and the fast aggregation of particles occurs. The high zeta value suggests that the NPs were stable with a high repulsive force. A higher value with nearly ± 30 mV is the limit value for setting the stability of the colloidal system [26,27].

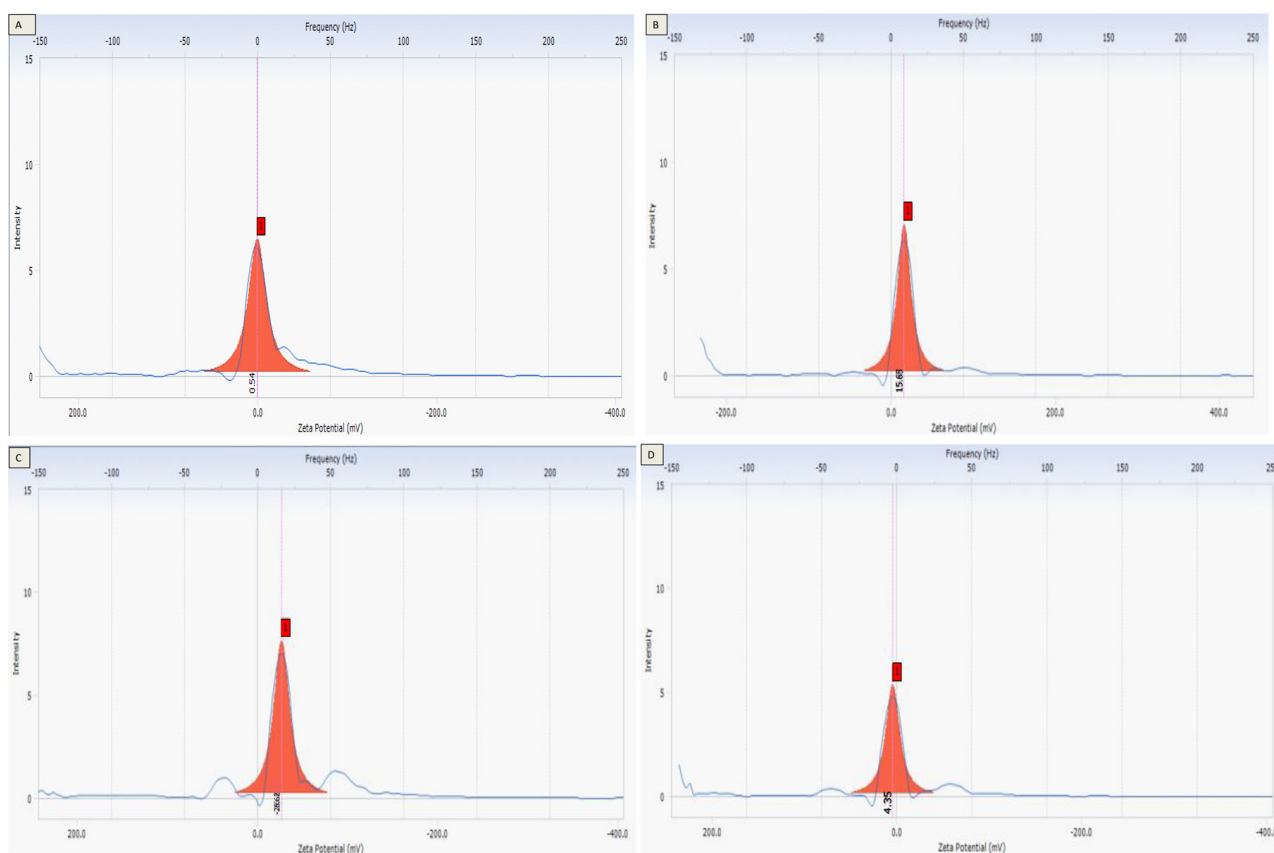


Figure 3. Zeta potential of (A) MNPs (B) ZCFNPs, (C) MNPs @ ZCFNPs, and (D) ZCFNPs @ MNPs.

3.3. Magnetic Behavior of the Nanostructures

The magnetic behavior was analyzed using VSM. The M-H plot exhibited hysteresis loops for the fabricated nanostructures, as shown in Figure 4. The magnetic parameters including coercivity (H_c), remanence magnetization (M_r), and saturation magnetizations (M_s) were taken from M-H plots and are listed in Table 3. The fabricated MNPs showed low coercivity (H_c) of 40.5 Oe, due to the existence of soft magnetic particles. ZCFNPs @ MNPs showed the highest saturation magnetization (M_s) of 59.30 emu/g. The retention of magnetism is important for the regeneration of the photocatalyst. Hybrid nanoparticles designed to merge the advantageous behavior of soft and hard phases showed outstanding magnetic behavior. The coercivity value of hybrid nanoparticles fell between the NPs and coated nanoparticles values. The magnetization of the nanostructure (ZCFNPs @ MNPs and MNPs @ ZCFNPs) was improved when compared to the nanoparticles (MNPs and ZCFNPs). The magnetization changed with the morphology and particle size of the nanoparticle until it reached a critical size, wherein the magnetization value was steady

and became near to the bulk value. M_s was lowered in the presence of magnetite soft coated in MNPs @ ZCFNPs when compared to the reversal nanostructure of ZCFNPs @ MNPs. The lower magnetization was due to the defect in the crystalline nanostructure with a small domain or the high oxidation degree non-magnetic phases [28–30]. The critical size for the superparamagnetic for CoFe_2O_4 via the size tuning (≈ 4 nm) and magnetization ($M_s \approx 30$ emu/g) was reported by Pereira et al. [31]. The coercivity values of nanostructure (CoFe_2O_4 @ MnFe_2O_4) and their inverse nanostructure with changing volume attribution were simulated by Song et al. [32]. It was detected that the magnetic behavior of the nanostructure was able to be controlled with the volume attribution of magnetic type. The high magnetization is considered significant in photocatalytic hydrogen production. In the absence of a magnetic field, the photo-catalysts should not possess a residual magnetism character to avert the collection of recycled photocatalysts for the following test. Photocatalysts can be removed using a magnetic bar in a suspended solution. Reduced remanence (SQ) is M_r/M_s . When SQ is higher than or equal to 0.5, the particles are single-domain structures, while below 0.5 are multi-domain structures. In this work, the SQ values were lower than 0.5, suggesting the existence of multi-domain structures [33].

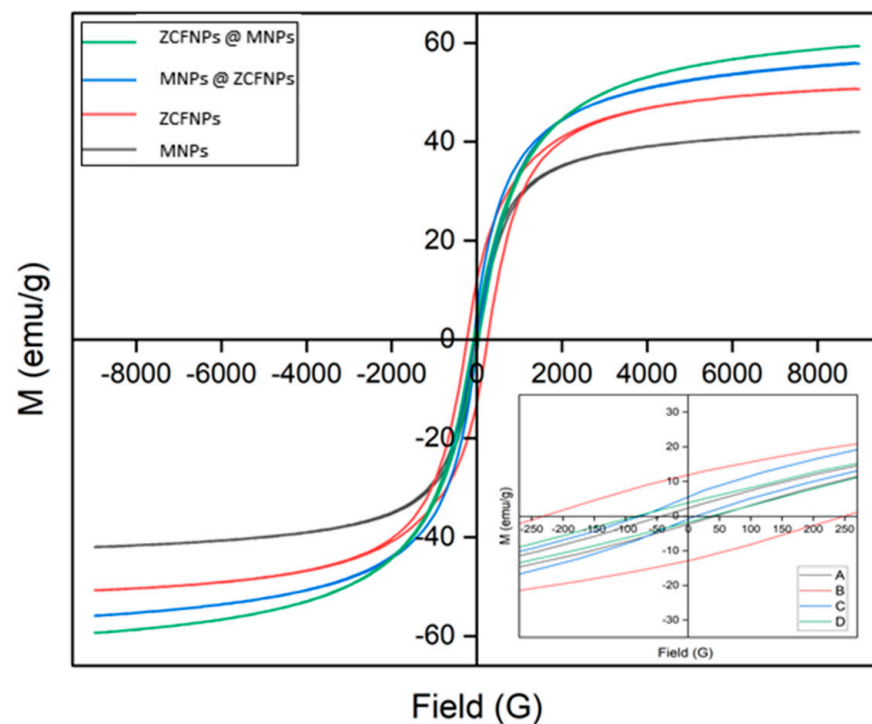


Figure 4. Magnetic properties of MNPs, ZCFNPs, MNPs @ ZCFNPs, and ZCFNPs @ MNPs.

Table 3. Magnetic properties of the prepared nanoparticles.

Sample	MNPs	ZCFNPs	MNPs @ ZCFNPs	ZCFNPs @ MNPs
M_s (emu/g)	41.93	50.71	55.75	59.30
M_r (emu/g)	3.8	10.71	6.8	6.3
H_c (Oe)	40.5	225	180	190
SQ	0.09	0.21	0.12	0.10

3.4. Photo Activity of the Fabricated Nanostructures

The electronic transition that occurs within atoms and molecules was studied using UV–VIS spectroscopy. The spectrum of the optical absorbance of the particles at ambient temperature is shown in Figure 5. The absorption property in the visible area originated

from the electronic charge transformation of Co^{2+} and Fe^{3+} to their conduction level in the conduction band. The spectra indicated a wide absorption range (300–600 nm) within the visible area, which may have been for the d-orbital transition. The peak was near 490 nm, which is related to the d-d transition of Fe^{3+} [34]. λ_{max} was observed at 490 nm, confirming that nano ferrite was active in the visible range. Band gap energy (E_g) was investigated from the spectra of absorption. In general, the electron transfer had the minimum required energy for the transitions. The band gap of the particle has the ability to excite and produce electrons and hole pairs for redox reactions to proceed. It is dependent on the dimensions, particle sizes, and shapes of the particles. To calculate the band gap, $(\alpha h\nu)^2$ was plotted against ' $h\nu$ '. The band gap energy is related to the absorption coefficient ' α ' by the Tauc equation:

$$(\alpha h\nu)^n = (\text{absorption coefficient} \times \text{energy})^n = (2.303Ah\nu)^n$$

A (constant), $h\nu$ (photon energy), n (= 2 for direct transition).

$$\text{Band gap energy } (E_g) = (hc)/\lambda$$

h : 6.626×10^{-34} Joules/s, c : 3.0×10^8 m/s, λ : cut off wavelength, $E_g = 1240 \text{ eV nm}/\lambda$

The band gap energies were calculated as 2.2, 2.4, 1.9, and 2.3 eV for MNPs, ZCFNPs, MNPs @ ZCFNPs, and ZCFNPs @ MNPs, respectively. As shown in Figure 5, for nanoparticles, MNPs and ZCFNPs, as the size increased from 10 to 25 nm, the band gap increased from 2.2 and 2.4 eV, respectively. In contrast, it was noticed for hybrid nanoparticles, MNPs @ ZCFNPs and ZCFNPs @ MNPs, that the crystallite size decreased from 9 to 8 nm, and the band gap increased from 1.9 to 2.3 eV, respectively. The band gap of the particle was tuned with a reverse relationship with particle size. This was the same as what has been observed in previous work [35]. The expected activity could be attributed to the possible changes in the band positions [36].

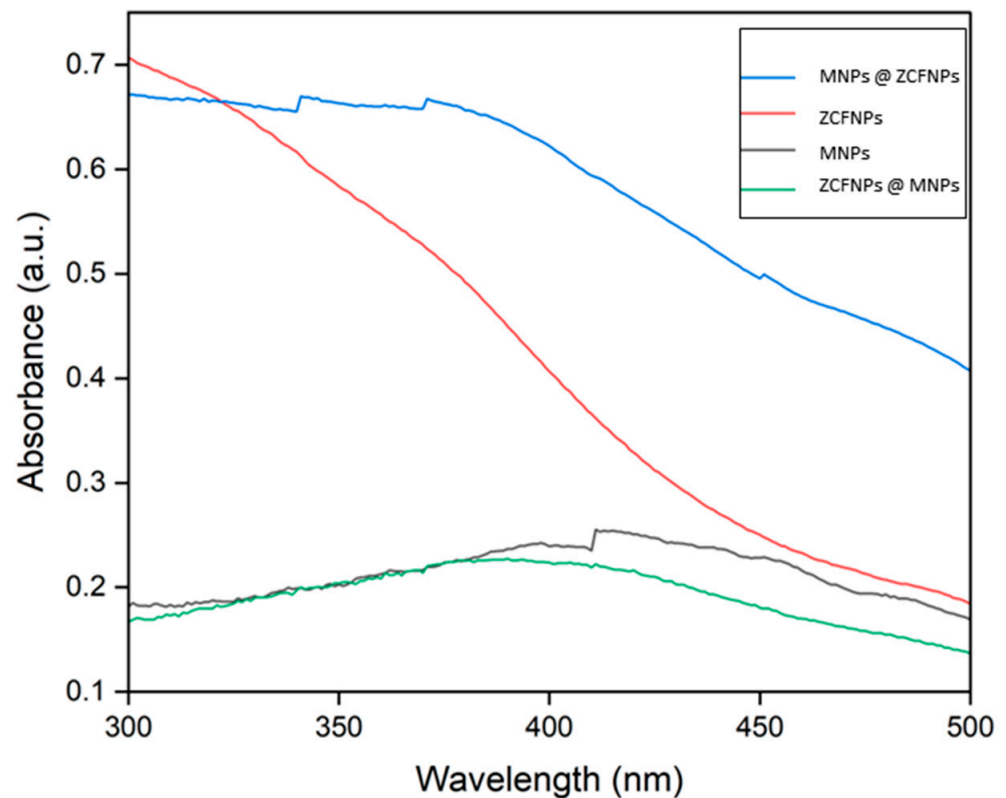


Figure 5. UV-VIS of MNPs, ZCFNPs, MNPs @ ZCFNPs, and ZCFNPs @ MNPs.

The photocatalytic behaviors of the prepared photocatalysts were investigated in the water-splitting system. The activity was measured in terms of the composition where the experiment was conducted under similar conditions. The energy was adsorbed by the magnetic photocatalyst, and then the electrons were migrated from the valence to the conduction band. If the band gap energy was enough and above that required for water splitting (1.23 eV), its band edge would fit the thermodynamics needed for the charge transfer to occur. So, the excited electrons were able to reduce hydrogen ions, and the hole was able to oxidize oxygen anions.

The hydrogen yield was measured at 60, 10, 24, and 1.4 mmole min⁻¹ g⁻¹ of photocatalyst for MNPs, ZCFNPs, MNPs @ ZCFNPs, and ZCFNPs @ MNPs, respectively, under magnetic force with visible light (Figure 6). The ability of iron oxide as a catalyst during the splitting of the water was able to lead to an enhancement. Hence, the tune of the layer composition was able to have a key part in the photocatalytic efficiency in terms of impacting the compositions of produced gases. The production of hydrogen by the prepared photocatalyst occurred through the following reactions: in the system of hydrogen production from water, they used a mixture solution of methanol and water. Through the photocatalytic system, the absorption of photons by the photocatalyst tends towards the promotion of an electron from the valence to conducting band, thus producing e⁻h⁺ pairs. In such a system, the proton's appearance occurred due to water/methanol oxidation through the radiation-produced holes. Protons were then involved in the process, by electrons, at the catalyst surface to produce hydrogen gas, as illustrated in Equation (1) [37].

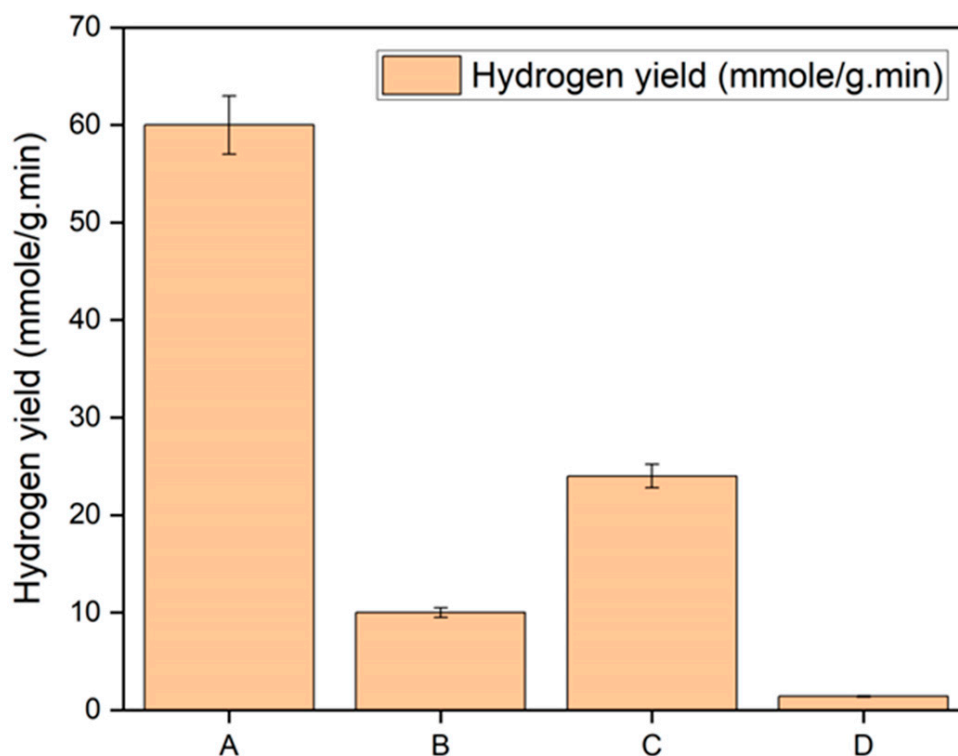
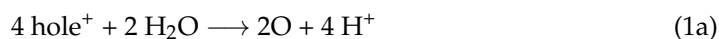
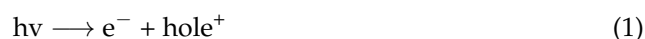


Figure 6. Hydrogen yields of (A) MNPs, (B) ZCFNPs, (C) MNPs @ ZCFNPs, and (D) ZCFNPs @ MNPs.

This methanol acted as a mediator in the oxidation process to avoid the reverse of oxygen that occurs due to water adsorption at the photo-catalyst. Methanol has been used to efficiently inhibit the function of re-grouping hole–electron pairs. In addition, methanol performed the role of a hole scavenger. Methanol could share in the production, as illustrated in Equations (2)–(4) [38].



The hydrogen yield for MNPs @ ZCFNPs was higher than 2.4-fold that of ZCFNP nanoparticles. In addition, the hydrogen yield for MNPs @ ZCFNPs was nearly 17-fold as compared to its reversal nanostructure ZCFNPs @ MNPs. MNPs showed the highest photocatalytic property among all the fabricated materials by decreasing the scattering of irradiation within the system. This may have been due to the redox behavior of ferrite nanoparticles, where the high yield was the result of both photo-catalytic as well as thermochemical water splitting. The hydrogen yield was almost non-existent without light and the photocatalyst.

The photocatalytic activity was influenced by the morphology and crystalline properties of the used nanoparticles [39,40]. The photocatalytic activity and magnetization of a TiO₂/SrFe₁₂O₁₉ photocatalyst could be altered by tuning the coated thickness [41]. Comparing the photocatalytic activity of the presented nanostructures with other nanostructures from previous work has been needed in order to investigate the efficiency of the photocatalysts in this work. Table 4 shows the yield by the prepared nanostructures and different photo-catalysts, as obtained from the other work.

Table 4. Hydrogen yield of current nanoparticles and previously reported structures.

Materials	Hydrogen Yield	Ref.
(CdS + ZnS)/Fe ₂ O ₃	4129 μmol	[1]
TiO ₂ /Fe ₂ O ₃	2700 μmol h ^{−1}	[2]
Zn _{0.8} Cd _{0.2} S@g-C ₃ N ₄	2351.18 μmol h ^{−1} g ^{−1}	[3]
Fe ₃ O ₄ @ZnS	3900 mmol h ^{−1} g ^{−1}	[4]
Fe ₃ O ₄ @ ZnCoFe ₂ O ₄	24 mmole min ^{−1} g ^{−1}	This work
ZnCoFe ₂ O ₄ @ Fe ₃ O ₄	1.4 mmole min ^{−1} g ^{−1}	This work

The presence of an external magnetic field can improve the photo-catalytic system via enhancing carrier transport and minimizing the re-combination [42–51]. It was reported that a magnetic field can inhibit the photo-induced charge recombination of ZnFe₂O₄, as the polarization can be controlled via magnetic fields, which improves the photoelectron chemical efficiency [44]. The magnetic field is considered to support the photocatalytic system by inducing the separation of photo-generated charges [44,45]. Lorentz force and microelectric potential are the main mechanisms of magnetic-assisted photo catalysis [46–50]. Hydrogen production via water utilizing a catalyst and solar energy is one of the most promising outlets for the production of clean and renewable energy. Photo catalysts should be stable, non-toxic, and economical visible light absorbers that are able to collect light photons with sufficient potential for water splitting. Here, we show that MNPs can meet these demands. These photocatalysts proved the ability to produce hydrogen efficiently. MNPs showed superior photocatalytic efficiency for hydrogen production when compared with other nanoparticles, allowing them to be favorable particles in the process. The high hydrogen yield by using the fabricated particles could depend on the magnetic behavior of those particles. The presence of magnetic behavior could acquaint the particles through

the system via magnetic forces. Consequently, the lowering of scattered radiation amounts in the system [51]. Also, electron spin polarization could lead to rapid migration of the particles and increased interactions between them. This confirms the relationship between the magnetic behavior of the photo-catalysts and their photo activity.

4. Conclusions

Magnetic photocatalysts based on MNPs, ZCFNPs, MNPs @ ZCFNPs, and ZCFNPs @ MNPs were fabricated successfully via a facile coprecipitation process. ZCFNPs @ MNPs showed the highest saturation magnetization: (M_s) 59.30 emu/g among all fabricated nanostructures. MNPs showed the highest hydrogen yield with 60 mmole $\text{min}^{-1} \text{g}^{-1}$, while ZCFNPs @ MNPs showed the lowest yield with 1.4 mmole $\text{min}^{-1} \text{g}^{-1}$. The hydrogen yield for MNPs @ ZCFNPs was more than 2.4-fold that of ZCFNP nanoparticles. Also, the hydrogen yield of MNPs @ ZCFNPs was nearly 17-fold, as compared to reversal nanostructure ZCFNPs @ MNPs. MNPs showed the highest photocatalytic property among all the fabricated nanostructures.

Funding: This research received no funding.

Data Availability Statement: The data is contained within the article.

Conflicts of Interest: The author declares no conflict of interest.

References

1. Preethi, V.; Kanmani, S. Photocatalytic hydrogen production using Fe_2O_3 -based core shell nano particles with ZnS and CdS. *Int. J. Hydrogen Energy* **2014**, *39*, 1613–1622. [[CrossRef](#)]
2. Madhumitha, A.; Preethi, V.; Kanmani, S. Photocatalytic hydrogen production using TiO_2 coated iron-oxide core shell particles. *Int. J. Hydrogen Energy* **2018**, *43*, 3946–3956. [[CrossRef](#)]
3. Tian, F.Y.; Hou, D.; Tang, F.; Deng, M.; Qiao, X.Q.; Zhang, Q.; Wu, T.; Li, D.S. Novel $\text{Zn}_{0.8}\text{Cd}_{0.2}\text{S}@g\text{-C}_3\text{N}_4$ core-shell heterojunctions with a twin structure for enhanced visible-light-driven photocatalytic hydrogen generation. *J. Mater. Chem. A* **2018**, *6*, 17086–17094. [[CrossRef](#)]
4. Chang, C.J.; Lee, Z.; Wei, M.; Chang, C.C.; Chu, K.W. Photocatalytic hydrogen production by magnetically separable $\text{Fe}_3\text{O}_4@\text{ZnS}$ and $\text{NiCo}_2\text{O}_4@\text{ZnS}$ core-shell nanoparticles. *Int. J. Hydrogen Energy* **2015**, *40*, 11436–11443. [[CrossRef](#)]
5. Patil, S.P.; Jagadale, S.A. Ferrites for electrocatalytic water splitting applications. In *Spinel Ferrite Nanostructures for Energy Storage Devices*; Elsevier: Amsterdam, The Netherlands, 2020; pp. 123–145.
6. Ye, Y.; Al-Khaleidi, N.; Barker, L.; Darwish, M.S.; El Nagggar, A.M.; El-Yahyaoui, A.; Hussein, A.; Hussein, E.S.; Shang, D.; Taha, M.; et al. Uranium resources in China's phosphate rocks—Identifying low-hanging fruits. *IOP Conf. Ser. Earth Environ. Sci.* **2019**, *227*, 052033. [[CrossRef](#)]
7. Saghafi, M.; Hosseini, S.A.; Zangeneh, S.; Moghanian, A.H.; Salarvand, V.; Vahedi, S.; Mohajerzadeh, S. Charge storage properties of mixed ternary transition metal ferrites MZnFe oxides ($\text{M} = \frac{1}{4} \text{Al, Mg, Cu, Fe, Ni}$) prepared by hydrothermal method. *SN Appl. Sci.* **2019**, *1*, 1303. [[CrossRef](#)]
8. Motawie, M.; Hanafi, S.A.; Elmelawy, M.S.; Ahmed, S.M.; Mansour, N.A.; Darwish, M.S.; Abulyazied, D.E. Wax co-cracking synergism of high density polyethylene to alternative fuels. *Egypt. J. Pet.* **2015**, *24*, 353–361. [[CrossRef](#)]
9. Darwish, M.S.A.; Kunz, U.; Peuker, U. Preparation and catalytic use of platinum in magnetic core/shell nanocomposites. *J. Appl. Polym. Sci.* **2013**, *129*, 1806–1811. [[CrossRef](#)]
10. Bhagwat, V.R.; Humbe, A.V.; More, S.D.; Jadhav, K.M. Sol-gel auto combustion synthesis and characterizations of cobalt ferrite nanoparticles: Different fuels approach. *Mater. Sci. Eng. B* **2019**, *248*, 114388. [[CrossRef](#)]
11. Darwish, M.S.A.; El-Sabbagh, A.; Stibor, I. Hyperthermia properties of magnetic polyethylenimine core/shell nanoparticles: Influence of carrier and magnetic strength. *J. Polym. Res.* **2015**, *22*, 239. [[CrossRef](#)]
12. Skoropata, E.; Desautels, R.D.; Chi, C.C.; Ouyang, H.; Freeland, J.W.; van Lierop, J. Magnetism of iron oxide based core-shell nanoparticles from interface mixing with enhanced spin-orbit coupling. *Phys. Rev. B.* **2014**, *89*, 024410. [[CrossRef](#)]
13. López-Ortega, A.; Estrader, M.; Salazar-Alvarez, G.; Roca, A.G.; Nogués, J. Applications of exchange coupled bi-magnetic hard/soft and soft/hard magnetic core/shell nanoparticles. *Phys. Rep.* **2015**, *553*, 1–32. [[CrossRef](#)]
14. Mangrulkar, P.A.; Joshi, M.M.; Tijare, S.N.; Polshettiwar, V.; Labhsetwar, N.K.; Rayalu, S.S. Nano cobalt oxides for photocatalytic hydrogen production. *Int. J. Hydrogen Energy* **2012**, *37*, 10462–10466. [[CrossRef](#)]
15. Chen, X.; Shen, S.; Guo, L.; Mao, S.S. Semiconductor-based photocatalytic hydrogen generation. *Chem. Rev.* **2010**, *110*, 6503–6570. [[CrossRef](#)] [[PubMed](#)]
16. Chen, X.; Li, C.; Grätzel, M.; Kostecki, R.; Mao, S.S. Nanomaterials for renewable energy production and storage. *Chem. Soc. Rev.* **2012**, *41*, 7909–7937. [[CrossRef](#)] [[PubMed](#)]

17. Artero, V.; Chavarot-Kerlidou, M.; Fontecave, M. Splitting water with cobalt. *Angew. Chem. Int. Ed.* **2011**, *50*, 7238–7266. [[CrossRef](#)]
18. An, W.-J.; Wang, W.-N.; Ramalingam, B.; Mukherjee, S.; Daubayev, B.; Gangopadhyay, S.; Biswas, P. Enhanced water photolysis with Pt metal nanoparticles on single crystal TiO₂ surfaces. *Langmuir* **2012**, *28*, 7528–7534. [[CrossRef](#)] [[PubMed](#)]
19. Jang, J.S.; Choi, S.H.; Kim, D.H.; Jang, J.W.; Lee, K.S.; Lee, J.S. Enhanced photocatalytic hydrogen production from water-methanol solution by nickel intercalated into titanate nanotube. *J. Phys. Chem. C* **2009**, *113*, 8990–8996. [[CrossRef](#)]
20. Nasrin, S.; Chowdhury, F.U.Z.; Hoque, S.M. Study of hyperthermia temperature of manganese-substituted cobalt nano ferrites prepared by chemical co-precipitation method for biomedical application. *J. Magn. Magn. Mater.* **2019**, *479*, 126–134. [[CrossRef](#)]
21. Darwish, M.S.A.; Kim, H.; Lee, H.; Ryu, C.; Lee, J.Y.; Yoon, J. Engineering core-shell structures of magnetic ferrite nanoparticles for high hyperthermia performance. *J. Nanomater.* **2020**, *10*, 991. [[CrossRef](#)]
22. Badawy, S.M.; Abd, E.-L. Synthesis and characterizations of magnetite nanocomposite films for radiation shielding. *Polym. Compos.* **2017**, *38*, 974–980. [[CrossRef](#)]
23. Angotzi, M.S.; Musinu, A.; Marni, V.; Ardu, A.; Cara, C.; Niznansky, D.; Xin, H.L.; Cannas, C. Spinel Ferrite Core-Shell Nanostructures by a Versatile Solvothermal Seed-Mediated Growth Approach and Study of Their Nanointerfaces. *ACS Nano* **2017**, *11*, 7889. [[CrossRef](#)] [[PubMed](#)]
24. Ayyappan, S.; Mahadevan, S.; Chandramohan, P.; Srinivasan, M.P.; Philip, J.; Raj, B. Influence of Co²⁺ Ion concentration on the size, magnetic properties, and purity of CoFe₂O₄ Spinel ferrite nanoparticles. *J. Phys. Chem. C* **2010**, *114*, 6334. [[CrossRef](#)]
25. Chinnasamy, C.N.; Senoue, M.; Jeyadevan, B.; Perales-Perez, O.; Shinoda, K.; Tohji, K. Synthesis of size-controlled cobalt ferrite particles with high coercivity and squareness ratio. *J. Colloid. Interface Sci.* **2003**, *263*, 80–83. [[CrossRef](#)] [[PubMed](#)]
26. Kmita, A.; Lachowicz, D.; Żukrowski, J.; Gajewska, M.; Szczerba, W.; Kuciakowski, J.; Zapotoczny, S.; Sikora, M. One-step synthesis of long term stable superparamagnetic colloid of zinc ferrite nanorods in water. *Materials* **2019**, *12*, 1048. [[CrossRef](#)] [[PubMed](#)]
27. Darwish, M.S.A.; Stibor, I. Pentenoic acid-stabilized magnetic nanoparticles for nanomedicine applications. *J. Dispers. Sci. Technol.* **2016**, *37*, 1793–1798. [[CrossRef](#)]
28. Choi, H.; An, M.; Eom, W.; Lim, S.; Shim, I.; Kim, C.; Kim, S.J. Crystallographic and magnetic properties of the hyperthermia material CoFe₂O₄@AlFe₂O₄. *Korean Phys. Soc.* **2017**, *70*, 173–176. [[CrossRef](#)]
29. Obaidat, I.M.; Issa, B.; Haik, Y. Magnetic properties of magnetic nanoparticles for efficient hyperthermia. *Nanomaterials* **2015**, *5*, 63–89. [[CrossRef](#)]
30. Zhen, G.B.; Muir, W.; Moffat, B.A.; Harbour, P.; Murray, K.S.; Moubaraki, B.; Suzuki, K.; Madsen, I.; Agron-Olshina, N.; Waddington, L.; et al. Comparative study of the magnetic behavior of spherical and cubic superparamagnetic iron oxide nanoparticles. *J. Phys. Chem. C* **2011**, *115*, 327–334. [[CrossRef](#)]
31. Pereira, C.; Pereira, A.M.; Fernandes, C.; Rocha, M.; Mendes, R.; Fernández-García, M.P.; Guedes, A.; Tavares, P.B.; Grenèche, J.M.; Araújo, J.P.; et al. Superparamagnetic MFe₂O₄ (M = Fe, Co, Mn) nanoparticles: Tuning the particle size and magnetic properties through a novel one-step coprecipitation route. *Chem. Mater.* **2012**, *24*, 1496–1504. [[CrossRef](#)]
32. Song, Q.; Zhang, Z.J. Controlled synthesis and magnetic properties of bimagnetic spinel ferrite CoFe₂O₄ and MnFe₂O₄ nanocrystals with core-shell architecture. *J. Am. Chem. Soc.* **2012**, *134*, 10182–10190. [[CrossRef](#)] [[PubMed](#)]
33. Prabhakaran, T.; Hemalatha, J. Combustion synthesis and characterization of cobalt ferrite nanoparticles. *Ceram. Int.* **2016**, *42*, 14113–14120. [[CrossRef](#)]
34. Mallick, P.; Dash, B.N. X-ray diffraction and UV-Visible characterizations of γ-Fe₂O₃ nanoparticles annealed at different temperature. *Nanosci. Nanotechnol.* **2013**, *3*, 130–134.
35. Anjum, S.; Tufail, R.; Rashid, K.; Zia, R.; Riaz, S. Effect of cobalt doping on crystallinity, stability, magnetic and optical properties of magnetic iron oxide nano-particles. *J. Magn. Magn. Mater.* **2017**, *432*, 198–207. [[CrossRef](#)]
36. Wender, H.; Gonçalves, R.V.; Dias, C.S.B.; Zapata, M.J.M.; Zagonel, L.F.; Mendonça, E.C.; Sérgio, R. Teixeira and Flávio Garcia Photocatalytic hydrogen production of Co(OH)₂ nanoparticle-coated α-Fe₂O₃ nanorings. *Nanoscale* **2013**, *5*, 9310–9316. [[CrossRef](#)] [[PubMed](#)]
37. Choi, H.-J.; Kang, M. Hydrogen production from methanol-water decomposition in a liquid photosystem using the anatase structure of Cu loaded TiO₂. *Int. J. Hydrogen Energy* **2007**, *32*, 3841–3848. [[CrossRef](#)]
38. Chen, J.; Ollis, D.F.; Rulken, W.H.; Bruning, H. Photocatalyzed oxidation of alcohols and organochlorides in the presence of native TiO₂ and metallized TiO₂ suspensions. Part (II): Photocatalytic mechanisms. *Water Res.* **1999**, *33*, 669–676. [[CrossRef](#)]
39. Fang, D.; Luo, Z.; Huang, K.; Lagoudas, D.C. Effect of heat treatment on morphology, crystalline structure and photocatalysis properties of TiO₂ nanotubes on Ti substrate and freestanding membrane. *Appl. Surf. Sci.* **2011**, *257*, 6451–6461. [[CrossRef](#)]
40. Hung, S.T.; Chang, C.J.; Hsu, C.H.; Chu, B.H.; Lo, C.F.; Hsu, C.C.; Pearton, S.J.; Holzworth, M.R.; Whiting, P.G.; Rudawski, N.G.; et al. SnO₂ functionalized AlGaN/GaN high electron mobility transistor for hydrogen sensing applications. *Int. J. Hydrogen Energy* **2012**, *37*, 13783–13788. [[CrossRef](#)]
41. Fu, W.; Yang, H.; Chang, L.; Bala, H.; Li, M.; Zou, G. Anatase TiO₂ nanolayer coating on strontium ferrite nanoparticles for magnetic photocatalyst. *Coll. Surf. A* **2006**, *289*, 47–52. [[CrossRef](#)]
42. Garcés-Pineda, F.A.; Blasco-Ahicart, M.; Nieto-Castro, D.; López, N.; GalánMascarós, J.R. Direct magnetic enhancement of electrocatalytic water oxidation in alkaline media. *Nat. Energy* **2019**, *4*, 519–525. [[CrossRef](#)]

43. Huang, H.J.; Wang, Y.H.; Chau, Y.F.C.; Chiang, H.P.; Wu, J.C.S. Magnetic Field-Enhancing Photocatalytic Reaction in Micro Optofluidic Chip Reactor. *Nanoscale Res. Lett.* **2019**, *14*, 323. [[CrossRef](#)] [[PubMed](#)]
44. Gao, W.; Peng, R.; Yang, Y.; Zhao, X.; Cui, C.; Su, X.; Qin, W.; Dai, Y.; Ma, Y.; Liu, H.; et al. Electron Spin Polarization-Enhanced Photoinduced Charge Separation in Ferromagnetic ZnFe₂O₄. *ACS Energy Lett.* **2021**, *6*, 2129–2137. [[CrossRef](#)]
45. Li, J.; Pei, Q.; Wang, R.Y.; Zhou, Y.; Zhang, Z.M.; Cao, Q.Q.; Wang, D.H.; Mi, W.B.; Du, Y.W. Enhanced photocatalytic performance through magnetic field boosting carrier transport. *ACS Nano* **2018**, *12*, 3351–3359. [[CrossRef](#)] [[PubMed](#)]
46. Li, J.; Yin, W.; Pan, J.; Zhang, Y.; Wang, F.; Wang, L.; Zhao, Q. External field assisted hydrogen evolution reaction. *Nano Res.* **2023**, *16*, 8638–8654. [[CrossRef](#)]
47. Li, H.D.; Sang, Y.H.; Chang, S.J.; Huang, X.; Zhang, Y.; Yang, R.S.; Jiang, H.D.; Liu, H.; Wang, Z.L. Enhanced ferroelectricnanocrystal-based hybrid photocatalysis by ultrasonic-wavegenerated piezophototronic effect. *Nano Lett.* **2015**, *15*, 2372–2379. [[CrossRef](#)] [[PubMed](#)]
48. Shi, Q.J.; Zhang, M.; Zhang, Z.M.; Li, Y.X.; Qu, Y.; Liu, Z.Q.; Yang, J.L.; Xie, M.Z.; Han, W.H. Energy and separation optimization of photogenerated charge in BiVO₄ quantum dots by piezo-potential for efficient gaseous pollutant degradation. *Nano Energy* **2020**, *69*, 104448. [[CrossRef](#)]
49. Gao, W.Q.; Lu, J.B.; Zhang, S.; Zhang, X.F.; Wang, Z.X.; Qin, W.; Wang, J.J.; Zhou, W.J.; Liu, H.; Sang, Y.H. Suppressing photoinduced charge recombination via the Lorentz force in a photocatalytic system. *Adv. Sci.* **2019**, *6*, 1901244. [[CrossRef](#)]
50. Gao, W.Q.; Liu, Q.L.; Zhang, S.; Yang, Y.Y.; Zhang, X.F.; Zhao, H.; Qin, W.; Zhou, W.J.; Wang, X.N.; Liu, H.; et al. Electromagnetic induction derived micro-electric potential in metalsemiconductor core–shell hybrid nanostructure enhancing charge separation for high performance photocatalysis. *Nano Energy* **2020**, *71*, 104624. [[CrossRef](#)]
51. Darwish, M.S.; El Nagggar, A.M.; Morshedy, A.S.; Haneklaus, N. Increased production of hydrogen with in situ CO₂ capture through the process of water splitting using magnetic core/shell structures as novel photocatalysts. *Environ. Sci. Pollut. Res.* **2021**, *28*, 3566–3578. [[CrossRef](#)]

Disclaimer/Publisher's Note: The statements, opinions and data contained in all publications are solely those of the individual author(s) and contributor(s) and not of MDPI and/or the editor(s). MDPI and/or the editor(s) disclaim responsibility for any injury to people or property resulting from any ideas, methods, instructions or products referred to in the content.